information

MDPI

Article

Symmetric Cross-Entropy: A Novel Multi-Level Thresholding Method and Comprehensive Study of Entropy for High-Precision Arctic Ecosystem Segmentation

Thaweesak Trongtirakul [1,*], Sos S. Agaian [2], Sheli Sinha Chauhuri [3], Khalifa Djemal [4] and Amir A. Feiz [5]

[1] Department of Electrical Power Engineering, Rajamangala University of Technology Phra Nakhon, Bangkok 10300, Thailand
[2] Graduate Center, City University of New York, New York, NY 10016, USA; sos.agaian@csi.cuny.edu
[3] Department of Electronics and Telecommunication Engineering, Jadavpur University, Kolkata 700032, India; sheli.sinha@jadavpuruniversity.in
[4] lnformatique, BIoinformatique et Systèmes Complexes (IBISC) Laboratory, University of Evry Paris-Saclay, 91020 Evry, France; khalifa.djemal@univ-evry.fr
[5] Laboratoire de Mécanique et d'Energétique d'Evry (LMEE), University of Evry Paris-Saclay, 91020 Evry, France; amirali.feiz@univ-evry.fr
* Correspondence: thaweesak.tr@rmutp.ac.th

Abstract

Arctic sea ice is a critical indicator of global climate dynamics, directly influencing maritime navigation, polar biodiversity, and offshore engineering safety. The precise mapping of diverse ice types, such as frazil ice, slush, melt ponds, and open water, is essential for environmental monitoring; however, it remains a formidable challenge in satellite remote sensing. These difficulties arise from low-contrast imagery, overlapping spectral signatures, and the subtle textural nuances characteristic of polar regions. Traditional entropy-based thresholding techniques often falter when segmenting these complex scenes, as they typically rely on Gaussian distribution assumptions that do not align with the stochastic nature of Arctic data. To address these limitations, this paper presents a novel unsupervised segmentation framework based on symmetric cross-entropy (SCE). Unlike standard directional measures, SCE provides a more robust objective function for multi-level thresholding by simultaneously maximizing intra-class cohesion and minimizing inter-class ambiguity. The proposed method uses an optimized search strategy to identify intensity levels that best delineate complex Arctic features. We conducted an extensive entropy-based comparative study that benchmarked SCE against 25 state-of-the-art entropy measures, including Shannon, Kapur, Rényi, Tsallis, and Masi entropies. Our experimental results demonstrate that the SCE method: (i) achieves superior accuracy by consistently outperforming established models in segmentation precision and boundary definition; (ii) provides visual clarity by producing segments with significantly reduced noise, making them ideal for identifying small-scale melt ponds and slush zones; and (iii) demonstrates computational robustness by providing stable threshold values even in datasets with non-Gaussian class distributions and poor illumination. Ultimately, these improvements deliver high-quality ice feature data that enhance risk assessment, operational planning, and predictive modeling. This research marks a major step forward in Arctic sea studies and introduces a valuable new tool for wider image processing and computer vision communities.

Keywords: Arctic sea ice; multi-level thresholding; symmetric cross-entropy; image segmentation; remote sensing; information theory

Academic Editor: Vincenzo Moscato

Received: 19 February 2026
Revised: 7 April 2026
Accepted: 9 April 2026
Published: 16 April 2026

1. Introduction

In recent decades, high-latitude environments have undergone rapid, fundamental structural and functional shifts driven by rising temperatures. On land, these include increased permafrost degradation, soil subsidence due to melting ground ice, the development of thermokarst terrain, extended and warmer growing seasons, and altered fire regimes [1–3]. Monitoring the Earth's surface is integral to a diverse array of global applications, including resource management [4], climate studies [5], agricultural planning [6], and urban development [7]. In remote sensing, automatic segmentation is a fundamental technique for isolating surface features from aerial and satellite imagery. The Arctic Ocean, with the longest coastline of any ocean on Earth, has recently been identified as one of the most vulnerable ecosystems to climate change [8]. This methodology is particularly critical in environmental science for monitoring polar regions, where Arctic sea ice influences global climate change, supports unique ecosystems, and dictates the feasibility of human activities. Therefore, rigorous differentiation between solid ice, melt ponds, and open water is a critical prerequisite. Such classification is fundamental to understanding climate variability and facilitating safe operations within the Arctic environment.

Also, the importance of improving our understanding of the Arctic, including coastal change, is widely recognized [8–11]. However, the remoteness of much of the Arctic and the difficulties of access make field-based mapping challenging. Additionally, persistent cloud cover, changing weather, and a short summer of about three months without snow or ice limit the ability to collect dense time series of remote sensing data, which are crucial for land surface and hydrological studies [8,12]. Developing reliable segmentation methods for accurate land cover mapping is equally important to having access to remote sensing images, because manually labeling images over large areas is not feasible on a regular schedule.

While optical imagery provides high-resolution data during the summer melt season, continuous year-round monitoring of the Arctic requires sensors capable of penetrating persistent cloud cover and operating during the polar night. Consequently, Synthetic Aperture Radar (SAR) and Global Navigation Satellite System Reflectometry (GNSS-R) have become indispensable tools for sea ice observation. Foundational research from Canadian institutions has significantly advanced these domains. Researchers at the University of Waterloo have developed robust classification models, such as Iterative Region Growing with Semantics (IRGS) and hierarchical neural networks, to map sea ice types and quantify concentration using dual-polarized SAR imagery [13,14]. Similarly, Memorial University has pioneered the application of GNSS-R techniques to retrieve sea ice thickness and altimetry, leveraging the sensitivity of reflected signals to surface roughness and permittivity [15,16]. While these microwave-based techniques offer broad temporal coverage, high-precision segmentation of high-resolution visible imagery remains essential for ground-truthing and analyzing fine-scale features like melt pond geometry, which is the primary focus of this work.

Classifying these Arctic elements accurately remains challenging. Arctic imagery often exhibits non-Gaussian class distributions and subtle brightness variations. This makes defining clear boundaries difficult. Although recent advances have improved land cover mapping methods, the availability of labeled data still poses a limitation. Deep neural networks usually require thousands of images for training, with the desired features already determined. Additionally, although deep learning models like Mask R-CNN deliver satisfying prediction accuracy, they rarely achieve real-time processing due to the need for numerous candidate bounding boxes and complex post-processing to eliminate redundant information [17]. At the same time, traditional segmentation methods include Otsu's thresholding, which is widely used due to its simplicity and effectiveness in maxi-

mizing between-class variance [18]. However, simple thresholding often struggles with specific scenarios involving complex textures and challenging lighting conditions typical of Arctic surfaces.

To address these complexities, entropy-based thresholding methods have been proposed as more flexible alternatives [19]. Examples include Shannon, Kapur, Rényi, Tsallis, and Masi entropy models [20–24]. Each model uses a different information-theoretic formulation to assess homogeneity within segmented regions or to evaluate randomness in the data. Entropy-based methods effectively quantify information content, making them useful for multimodal histograms that often feature undefined class boundaries. Nevertheless, traditional entropy-based thresholding methods struggle with highly complex scenes [25,26].

This paper introduces the symmetric cross-entropy (SCE) multi-level thresholding algorithm to overcome these challenges. The proposed method integrates a cosine–logarithmic transformation into a unified equation for self-enhancement. Subsequently, the algorithm employs a novel, optimized thresholding technique that relies on local-minima analysis of the smoothed histogram, diverging from standard brute-force search methods. The optimal threshold is determined by maximizing a unique symmetric cross-entropy (SCE) measure, which, by incorporating a symmetric log–cosine function, quantifies the divergence between the original and smoothed histogram distributions.

Key Contributions

- Novel Optimization Approach: We introduce an objective function defined using a symmetric log–cosine entropy measure. This method restricts the search space to a local minimum, ensuring thresholds are placed in regions of low pixel density to effectively separate classes.
- Enhanced Arctic Segmentation: The proposed method excels at segmenting complex Arctic imagery, significantly improving accuracy for features like ice/slush, melt ponds, and open water.
- Superior Performance: Experimental results demonstrate that the proposed SCE method outperforms advanced models based on Shannon, Kapur, Rényi, Tsallis, and Masi entropies, producing more accurate, visually clear segments with well-defined boundaries.

The remainder of this paper is structured as follows: Section 2 reviews the background of entropy-based segmentation techniques in Arctic sea research. Section 3 introduces the proposed Multi-Level Entropy-Based Thresholding for Enhanced Segmentation framework and details its methodology. Section 4 evaluates the method's performance using both quantitative metrics and visual inspection. Finally, Section 5 offers a discussion and a conclusion.

2. Background

Image segmentation approaches are generally categorized into two primary classes: traditional methods and deep learning techniques. Traditional methods encompass a wide range of algorithms, including edge detection, fuzzy logic, morphological operations, region growing, partial differential equations (PDEs), graph-based formulations, and thresholding. On the other hand, deep learning methods leverage the distinct representational power of neural networks, supported by large-scale annotated datasets and advancements in hardware that make training deep architectures feasible. While deep neural networks have achieved state-of-the-art performance, their success is heavily dependent on the availability of diverse and representative training data. Without such data, adopting complex methodologies becomes necessary. Approaches such as transfer learning,

data augmentation, or class balancing techniques may be employed. Unfortunately, each method brings its own set of implementation challenges.

Thresholding methodologies offer a competitive alternative in data-scarce contexts. These methods eliminate the need for time-consuming training stages, unlike deep learning approaches. Furthermore, their parameterization is simpler than that of active contour models or graph formulations. The formulation of thresholding is also intuitive. This simplicity enables the development of algorithms with lower computational complexity than PDE-based methods. Such advantages have sustained research into thresholding. This is evidenced by recent applications in thermograms, medical imaging, satellite imagery, and color images.

Among the various thresholding categories classified by [27], entropy-based methods have garnered significant attention due to their robust theoretical foundation in information theory and statistical mechanics.

The history of entropy traces progression from macroscopic observations to microscopic understanding, and ultimately to an algorithmic perspective [28]. As illustrated in Figure 1, the concept of entropy originated in the 19th century with Rudolf Clausius, who defined it as a measure of energy dissipation in thermodynamic systems. This physical viewpoint was further developed by Ludwig Boltzmann and J. Willard Gibbs, who employed statistical mechanics to connect entropy with the microscopic disorder of atoms.

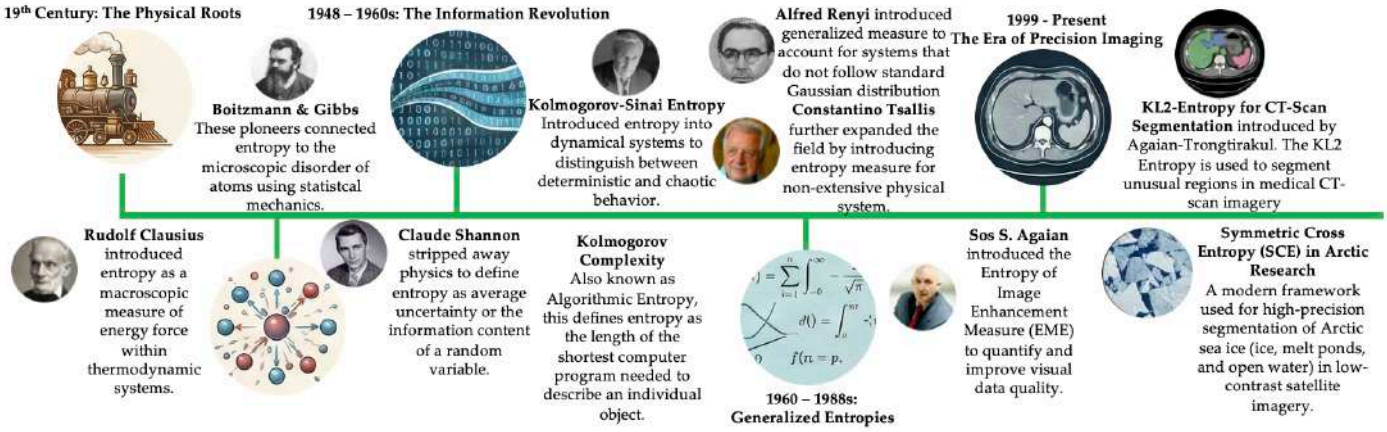

Figure 1. Evolution of entropy: from steam engines to precision imaging.

In 1948, Claude Shannon revolutionized the field by stripping away physics and redefining entropy as "information content" or the average uncertainty of a random variable. However, it was Andrey Kolmogorov in the late 1950s and 60s who provided two of the most profound modern extensions: first, the Kolmogorov–Sinai entropy, which introduced entropy into the study of dynamical systems to distinguish between deterministic and chaotic behavior [29,30]; and second, the concept of Kolmogorov complexity (Algorithmic Entropy) [31]. By defining the entropy of an individual object as the length of the shortest computer program required to describe it, Kolmogorov shifted the focus from "average uncertainty" to "absolute randomness." This fundamental distinction between the probabilistic nature of Shannon entropy and the algorithmic nature of Kolmogorov complexity is summarized in Table 1.

Following the above foundational work, the field expanded into **generalized entropies**, with scholars such as Alfréd Rényi and Constantino Tsallis introducing parameterized measures, such as the Rényi and Tsallis entropies, to account for non-extensive and non-Gaussian systems.

Table 1. Comparison between Shannon entropy and Kolmogorov complexity.

Feature	Shannon Entropy (H)	Kolmogorov Complexity (K)
Fundamental Nature	Statistical/probabilistic	Algorithmic/deterministic
Subject of Measure	A random variable (source) or probability distribution	An individual object (e.g., a specific binary string)
Definition	The average uncertainty or information content of a source	The length of the shortest computer program required to generate the object
Mathematical Model	$H(x) = -p(x)\log(p(x))$	$K(x) = \min\{\|k\| : U(k) = x\}$
Perspective	Average case: expected value over all possible outcomes	Individual case: structural complexity of a single instance
Computability	Computable (given the probability distribution)	Generally incomputable (due to the halting problem)
Interpretation of Randomness	Unpredictability of the source	Incompressibility of the string

While generalized entropies like Rényi and Tsallis improved thresholding for non-extensive systems, they remained dependent on global histogram statistics, often ignoring local spatial structures. This limitation led to the development of "precision imaging" entropies designed to quantify local features and structural complexity [32]. A foundational measure in this era is the Entropy of Image Enhancement Measure (EME), introduced by Agaian [33]. Unlike varying global probabilistic measures, EME divides an image into localized blocks ($k_1 \times k_2$) and computes the logarithmic ratio of maximum to minimum intensities within each block. This approach effectively mimics the Human Visual System (HVS) by quantifying local contrast and dynamic range rather than just pixel frequency. Later, Agaian and Trongtirakul introduced the KL2-Entropy, a divergence-based metric tailored for medical imaging [34]. By modifying the classical Kullback–Leibler divergence, KL2-Entropy enhances the sensitivity to "unusual" or distinct regions within an image, such as anomalies in CT scans. These precision measures marked a paradigm shift: moving from simple information counting to algorithmic definitions that capture the semantic quality and spatial distribution of image data. This evolution sets the stage for the symmetric cross-entropy (SCE) proposed in this study, which leverages symmetric logarithmic divergence to resolve the overlapping spectral signatures of Arctic ice types.

Entropy-based methodologies are diverse. They cater to specific analytical needs across various disciplines, as illustrated in Figure 2. Entropy-based measures can be divided into three key categories: core information and distribution measures; structural and dynamic measures; and specialized and emerging applications. The first category encompasses foundational metrics like Shannon entropy. It also includes parametric generalizations like Renyi and Tsallis entropy. These metrics are essential for quantifying diversity in complex systems. The second category extends entropy concepts to relational data. It also covers time-dependent sequences. Key examples include graph and temporal entropy. Finally, the measures in the last category highlight advanced implementations. For instance, fuzzy entropy handles ambiguity. KL2-Entropy aids in specific tasks like CT-scan segmentation. Together, they demonstrate the adaptability of entropy in solving domain-specific problems.

The fundamental principle of these methods is to interpret the normalized image histogram as a probability distribution, $P = \{p_1, p_2, \ldots, p_L\}$, where p_i represents the probability of the i-th intensity level. The objective is to select thresholds that maximize the information content of the separated regions.

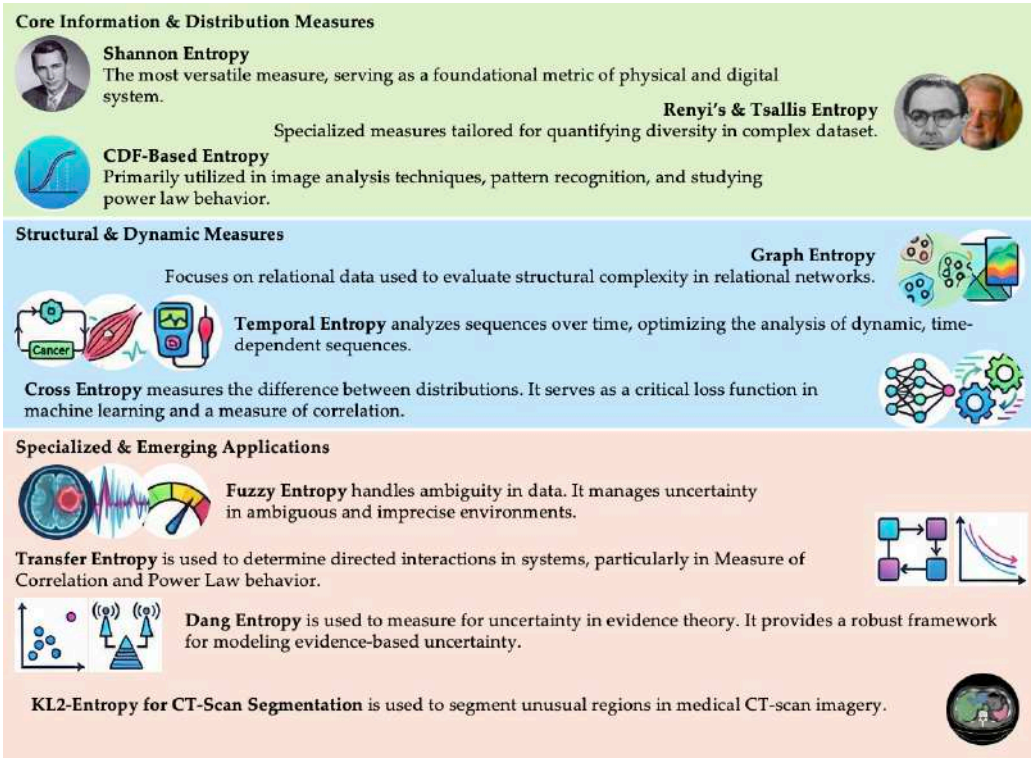

Figure 2. Overview of entropy measures categorized by their fundamental nature and domain-specific applications.

The application of entropy to image thresholding was introduced by Pun [35] and refined by Kapur et al. [36] using Shannon entropy. They utilized Shannon entropy (H_S), which is a measure of average information content. Shannon entropy characterizes extensive systems, which exhibit the property of additivity. This implies that the total entropy is the summation of the constituent parts. It is calculated as follows:

$$H_S = -\sum_{i=1}^{L} p_i \log(p_i), \tag{1}$$

Assuming that the histogram is separated into several parts, $H_0, H_1, \ldots, H_n$, by a set of thesholds, $t_0, t_1, \ldots, t_{n-1}$, the corresponding entropies are defined as

$$\begin{cases} H_0 = -\sum_{i=1}^{t_0} p_i \log(p_i) \\ H_1 = -\sum_{i=1}^{t_1} p_i \log(p_i) \\ \vdots \\ H_n = -\sum_{i=t_{n-1}}^{L} p_i \log(p_i) \end{cases}, \tag{2}$$

The objective function is given by the sum of H_n. It defined as

$$\psi(t) = \sum_{i=1}^{n} H_i, \tag{3}$$

The optimal set of thresholds is calculated as

$$t* = \underset{t \in \{t_0, t_1, \ldots, t_n\}}{\operatorname{argmax}} \ \psi(t), \tag{4}$$

Although effective for images with distinct modes, Shannon-based methods have limitations. They can yield identical results for different images with the same histogram, and they lack the tunable sensitivity needed for complex textures.

To address the limitations of the fixed Shannon measure, researchers introduced parametric entropies that offer greater flexibility. Sahoo et al. [37] adapted Renyi entropy, which generalizes the Shannon measure by introducing an entropic parameter $\alpha; \alpha \neq 1$. It is defined as

$$H_R(\alpha) = \frac{1}{1-\alpha} - \sum_{i=1}^{L} \log(p_i^{\alpha}), \tag{5}$$

Renyi entropy allows for adjustment of the sensitivity to the probability distribution's shape. In the limit of $\alpha \to 1$, H_R converges to the Shannon entropy, H_S. A major shift occurred with the introduction of non-extensive statistical mechanics by Tsallis [38,39]. Tsallis entropy (H_T) is defined by the entropic index $q; q \neq 1$. It is defined as

$$H_T(q) = \frac{1}{q-1}\left(1 - \sum_{i=1}^{L} \log\left(p_i^{q}\right)\right), \tag{6}$$

In image processing, Tsallis entropy is particularly effective for systems exhibiting complex pixel interdependencies. These dependencies often manifest as intricate, non-random textures. This method contrasts with Shannon entropy. Shannon entropy assumes a level of statistical independence. However, this assumption may not hold for complex natural images.

However, while Tsallis entropy offers flexibility, it deviates from the logarithmic form of standard information theory. Masi entropy [40] resolves this by modifying the Shannon measure to include a tunable parameter $r; (r \neq 1)$ while preserving the logarithmic additivity. It is defined as

$$H_M(r) = \frac{1}{1-r}(\log(1 + (1-r)H_s)), \tag{7}$$

where H_s is the standard Shannon entropy. The limit $r \to 1$ recovers the Shannon measure.

The histogram analysis in Figure 3 highlights the instability of relying on a single entropic measure. The resulting thresholds span a wide range $(t = 34 - 135)$. It demonstrates that indices respond to different statistical features. Masi and Shannon represent the lower bound, which is sensitive to local maxima in dark regions. Otsu and Kapur establish the threshold in the valley between local-minima regions, while Renyi and Tasallis shift toward the dominant pixel population at the higher end.

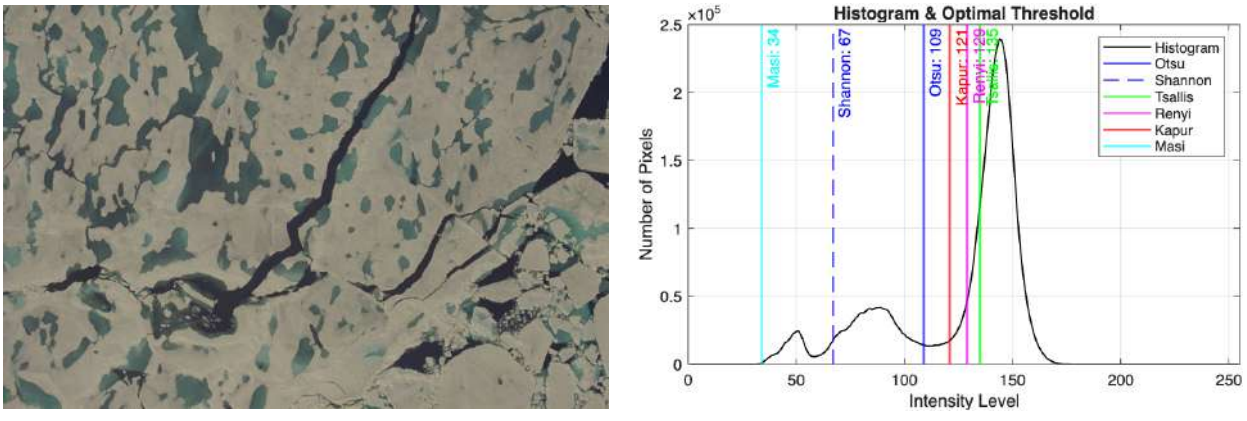

(**a**) (**b**)

Figure 3. Comparison of different thresholding techniques applied to an ice sheet image: (**a**) original Arctic sea ice image, and (**b**) comparison of optimal thresholds on the image histogram: Shannon (t = 67), Kapur (t = 121, Otsu (t = 109), Rényi (t = 129), Tsallis (t = 135), and Masi (t = 34).

To address the distinction between the long-range and short-range sensitivity entropy models, we introduce a cosine–logarithmic integration. By implementing a joint optimization framework [41], the proposed approach utilizes the flexibility of Kapur entropy to handle intricate correlation structures.

3. Proposed Method

The proposed method for multi-level image segmentation utilizes an optimized thresholding technique based on local-minima analysis and a hybrid cross-entropy maximization criterion. To accurately map the Arctic surface, we define three primary target classes: ice/snow, melt ponds (including slush), and open water.

As slush represents a physical transition with spectral characteristics that overlap with both shallow melt ponds and saturated ice, isolating it as an independent fourth class via 1D intensity-based thresholding can lead to boundary instability. By consolidating slush and melting ponds into a single region of interest, the algorithm mitigates noise while maintaining structural integrity. Accordingly, the segmentation process is optimized to calculate the optimal thresholds $K = 2$, effectively partitioning the intensity histogram into three distinct zones (C_1, C_2, and C_3).

3.1. Image Preprocessing and Histogram Computation

Let $\boldsymbol{I}$ denote the input color image. To facilitate intensity-based segmentation, the image is first converted to grayscale representation, I_x, where pixel values are normalized to the range $[0,\ 1]$. The probability density function of the image intensity levels is computed using a normalized histogram. Let h_i represent the count of pixels at intensity level i, where $i \in [0,\ 255]$, and N represents the total number of pixels. The probability density function is defined as

$$P_i = \frac{h_i}{N}, \tag{8}$$

3.2. Histogram Smoothing and Local Minima Identification

To reduce noise and identify significant structural features within the histogram, a smoothing operation is applied. Unlike determining thresholds by brute-force searching all intensity levels as seen in the standard Otsu methods, the proposed method restricts the search space to the local minima of the smoothed histogram. We apply a moving median filter to P_i with a kernal size of w to generate a smoothed probability density function, S_i. It can be calculated as

$$S_i = \text{median}(P_k) \quad \text{for} \quad i - \frac{w-1}{2} \leq k \leq i + \frac{w-1}{2}, \tag{9}$$

The candidate thresholds, T_c, are identified by locating the local minima of S_i. By restricting the optimal threshold search to these valley points, the algorithm ensures that thresholds are placed in regions of low pixel density.

In this study, to partition the image into the three primary functional zones (ice/snow, melt ponds/slush, and open water), we set $K = 2$ thresholds. This choice ensures that the intensity histogram is divided into three distinct operational regions.

Furthermore, the algorithm applies a moving median filter to the image histogram, using a kernel size of w, to generate a smoothed probability density function. The parameter w is determined empirically based on the dataset's quantization noise. A kernel size that is too small fails to eliminate spurious peaks, leading to an excess of false candidate thresholds. In contrast, an excessively large kernel over-smooths the histogram, potentially obscuring the narrow valleys that define critical class boundaries.

Figure 4 visually demonstrates this trade-off. For the high-resolution HOTRAX dataset, a kernel size of $w = 5$ was found to provide the optimal balance, effectively suppressing localized noise while preserving the distinct macroscopic valleys necessary for accurate threshold placement.

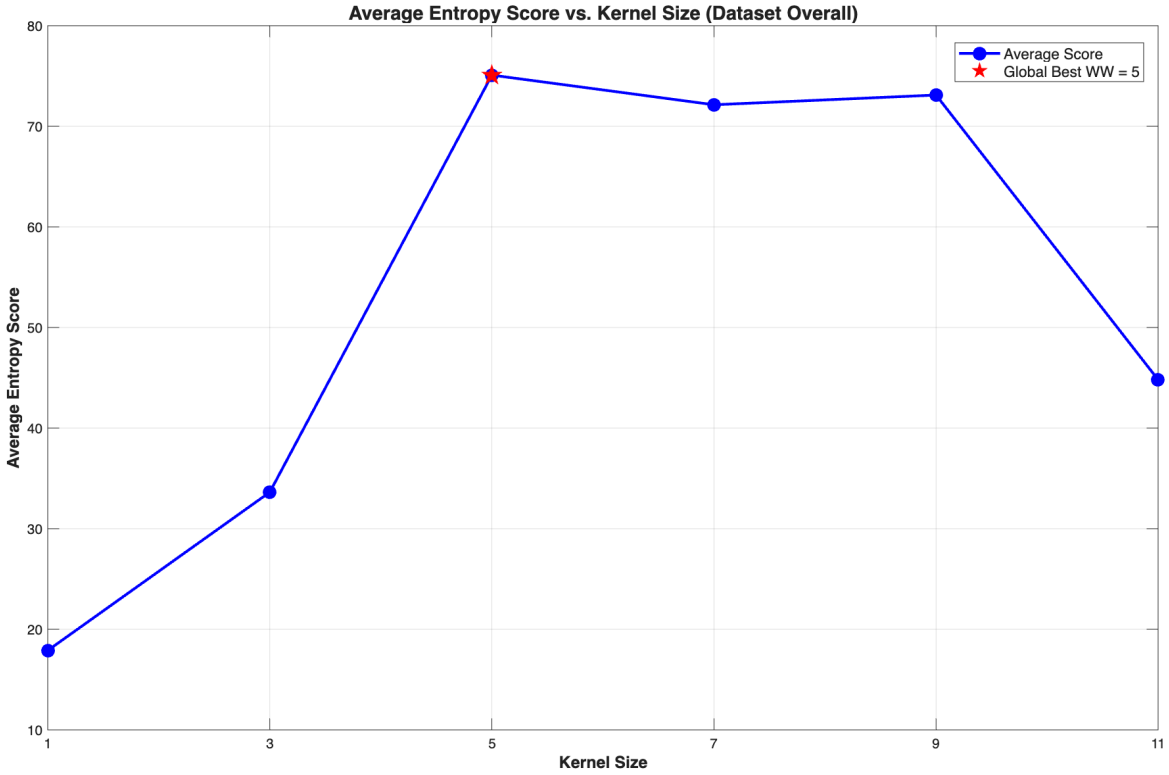

Figure 4. Impact of smoothing kernel size (w) on histogram characteristics and kernel threshold selection. Smaller kernels (e.g., $w = 3$) retain excessive noise, while larger kernels (e.g., $w = 11$) obscure critical valleys. The optimal range ($w = 5$ or $w = 7$) preserves key boundaries.

3.3. Symmetric Cross-Entropy Maximization and Threshold Optimization

To select the optimal threshold from T_c, we utilized a cross-entropy maximization approach. For a desired number of thresholds, K, the algorithm evaluates all possible combinations of K minima. For a specific combination of thresholds partitioning the histogram into distinct intervals, the similarity between the original probability density function, P_i, and the smoothed probability density function, S_i, is measured. The objective function, J, for a given interval, $[a, b]$, is defined using a symmetric log–cosine function as

$$J = \sum_{i=a}^{b} \left[\left(\cos\left(\log\left(\frac{2p'_i + 1}{p'_i + s'_i + 1} \right) \right) \right)^{-1} + \left(\cos\left(\log\left(\frac{2s'_i + 1}{p'_i + s'_i + 1} \right) \right) \right)^{-1} \right], \quad (10)$$

where p'_i and s'_i are the locally normalized probabilities within a specific interval $[a, b]$. The optimal threshold set, $t*$, is the combination that maximizes the summation of J across all intervals. The complete computational procedure is detailed in Algorithm 1.

Algorithm 1: Optimized Local-Minima Cross-Entropy Thresholding

Input: Grayscale image, $I_{x,y}$
Number of thresholds, n.
Smoothing kernel size, w.
Output: Set of optimal thresholds, $t*$.
Compute normalized histogram: $P_i \leftarrow \frac{h_i}{N}$.
Apply a moving median filter: $S_i \leftarrow \text{median}(P_k)$ for $i - \frac{w-1}{2} \leq k \leq i + \frac{w-1}{2}$
Initialize a candidate threshold: $t_c \leftarrow \varnothing$
For $i = 1$ to $H - 2$ **do** where H denotes the total intensity levels in the image, $I_{x,y}$.
  If $S_{i-1} > S_i$ **and** $S_{s+1} > S_i$
    Append i to t_c: $t_c \leftarrow i$
  End
End
Generate all combinations τ of size n from t_c.
Initialize a maximum entropy score: $J_{max} \leftarrow -\infty$
For each combination t **in** τ do
  Sort t and defined intervals $[a, b]$ based on $[0, t_1, t_2, \ldots, H]$.
  Initialize the current entropy score: $J_i \leftarrow 0$
  For each interval $[a, b]$ defined by t **do**
    Calculate local probabilities P_i and S_i
    Normalize P_i and S_i: $p'_i \leftarrow \frac{P_i}{\sum_i P_i}$ and $s'_i \leftarrow \frac{S_i}{\sum_i S_i}$
    Compute the log-cosine entropy:

$$J \leftarrow \sum_{i=a}^{b} \left[\left(\cos\left(\log\left(\frac{2p'_i + 1}{p'_i + s'_i + 1} \right) \right) \right)^{-1} + \left(\cos\left(\log\left(\frac{2s'_i + 1}{p'_i + s'_i + 1} \right) \right) \right)^{-1} \right]$$

    Update the current entropy score: $J_i \leftarrow J_i + J$
  End
  If $J_i > J_{max}$
    Update the set of optimal thresholds: $t* \leftarrow t$
  End
End
Return $t*$

3.4. Segmentation and Visualization

Once the optimal thresholds, $t*$, are determined in Algorithm 1, the scalar quantization of the image is performed. Pixels are labeled according to the intervals defined by the thresholds as

$$L_{x,y} = k \quad \text{if} \quad t_{k-1} < I_{x,y} \leq t_k, \tag{11}$$

where $L_{x,y}$ represents the label of the pixel. Finally, the segmented regions are visualized by mapping these labels to a user-defined colormap (e.g., red, green, and blue for $K = 2$) and creating a transparent overlay on the original image to facilitate visual inspection of the segmented structures.

4. Computer Simulation Results and Discussion

We implemented the proposed approach using MATLAB 2025b on a personal computer equipped with an Apple M2 Pro processor, 16 GB of memory, and macOS Tahoa 26.0.1.(Manufacturer: Apple Inc. City: Cupertino, CA, Country: USA) To demonstrate the efficacy of this method, we performed experiments on the publicly available Healy–Oden

Trans Arctic Expedition (HOTRAX) dataset [42], which is utilized for ice sheet detection in visible imagery. Specifically, we selected images 495, 502, 507, 508, 509, 513, 514, 1816, 1985, and 1987, as shown in Figure 5.

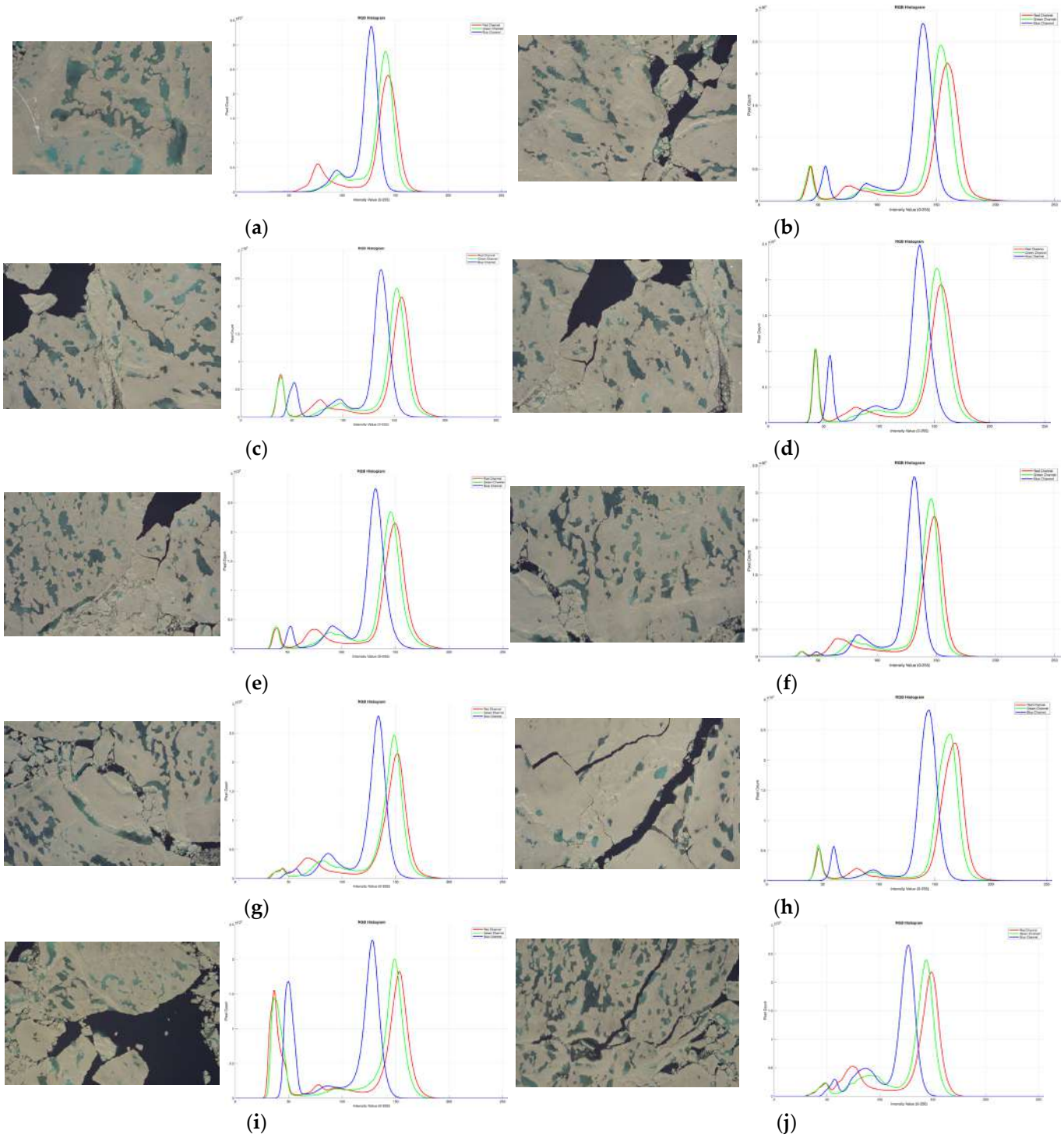

Figure 5. Examples of the HOTRAX dataset and their histograms, named (**a**) 495, (**b**) 502, (**c**) 507, (**d**) 508, (**e**) 509, (**f**) 513, (**g**) 514, (**h**) 1816, (**i**) 1985, and (**j**) 1987.

To ensure a fair comparison, we applied the same preprocessing procedure—specifically, grayscale conversion—to all methods prior to segmentation. We then compared the proposed algorithm against various entropy-based image thresholding methods, including Shannon [43], Tsallis [44], Renyi [45], Kapur [46], and Masi [24].

4.1. Dataset

We used the MeltPondNet dataset, a detailed collection of high-resolution aerial images tailored for Arctic sea ice feature detection and melt pond identification detection. The imagery was acquired during the Healy–Oden Trans Arctic Expedition (HOTRAX), conducted from 5 August to 30 September 2005. Images were captured from a helicopter using a Nikon D70 digital camera at altitudes ranging from 150 to 700 m to minimize interference from low cloud cover.

The dataset comprises high-resolution Arctic sea ice imagery featuring ice floes, melt ponds, and open water. It is important to clarify that while slush is a physical component of the summer melt cycle, its spectral intensity in visible-band imagery heavily overlaps with surrounding features. To ensure algorithmic robustness and avoid over-segmentation noise, this study merges "slush" and "melt ponds" into a consolidated class.

The differentiation presented in this work, therefore, focuses on three primary functional categories: solid ice/snow, melt ponds (including slush), and open water. The technical specifications of the dataset are as follows:

- Image Resolution: 3042 $\times$ 2048 pixels per image.
- Spatial Resolution: 5 to 25 cm per pixel, varying with flight altitude.
- Geographic Coverage: Central Arctic Ocean during the summer melt season.

4.2. Quantitative Evaluation

To objectively assess the segmentation quality, we conducted a comprehensive quantitative analysis using eight standard performance metrics—boundary F1 (BF) score, Dice similarity coefficient, Jaccard index, accuracy, precision, and recall—as listed in Table 2. The proposed method was benchmarked against six established thresholding techniques, Otsu, Shannon, Kapur, Masi, Renyi, and Tsallis, across ten test images from the HOTRAX dataset.

Table 2. Summary of quantitative evaluation metrics [47,48].

Metric	Mathematical Formulation	Description
Pixel Accuracy	$Accuracy = \frac{TP+TN}{TP+TN+FP+FN}$	Measures the ratio of correctly classified pixels (both foreground and background) to the total number of pixels.
Precision	$Precision = \frac{TP}{TP+FP}$	Evaluates the proportion of true positive pixels among all pixels classified as the region of interest; indicates the level of background noise suppression.
Recall (Sensitivity)	$Recall = \frac{TP}{TP+FN}$	Measures the ability of the algorithm to capture the complete region of interest (ROI) without under-segmentation.
Dice Similarity Coefficient (DSC)	$DSC = \frac{2TP}{2TP+FP+FN}$	Evaluates the spatial overlap between segmentation results and the ground truth.
Jaccard Index (IoU)	$Jaccard = \frac{TP}{TP+FP+FN}$	Confirms that the segmentation results are structurally closer to the ground truth.
Boundary F1 (BF) Score	$BF\ Score = \frac{2P_b \cdot R_b}{P_b+R_b}$	Evaluates the accuracy of the contour definition using boundary precision (P_b) and boundary recall (R_b) within a specific distance tolerance.

4.2.1. Evaluation Metrics

To validate segmentation performance, we use pixel-level confusion matrix statistics. Let G represent the ground-truth image and S denote the segmentation result. We define true positives (TP) as pixels correctly classified as the region of interest, false positives (FP)

as background pixels incorrectly classified as the region, false negatives (FN) as region pixels incorrectly classified as background, and true negatives (TN) as correctly classified background pixels. The mathematical formulations and detailed descriptions of the six evaluation metrics used in this study, pixel accuracy, precision, recall, Dice similarity coefficient (DSC), Jaccard index (IoU), and boundary F1 (BF) score, are comprehensively summarized in Table 2.

4.2.2. Boundary Displacement Error

This is a critical metric for evaluating how accurately a segmentation algorithm delineates the contours of the region of interest (ROI). A higher BF score indicates a closer match between the computed boundary and the ground truth.

Table 3 presents the comparative results of the proposed method against six established algorithms. The proposed method demonstrates a distinct superiority in contour definition. It consistently achieves scores above 0.93 across all ten test images. The proposed method exhibits remarkable stability compared to conventional entropy-based methods. For instance, the Shannon and Kapur algorithms show significant fluctuations. They drop as low as 0.1450 (Image 508) and 0.2252 (Image 495), respectively. The proposed method maintains high precision. The peak is 0.9953 for Image 509. It is evident that the proposed algorithm is robust against image variations that typically degrade the performance of entropy maximization techniques.

Table 3. Quantitative evaluation of segmentation performance using the BF score metric. *Note: The best score in each row is highlighted in green bold, while the second-best score is highlighted in blue.*

Image No.	Otsu	Shannon	Kapur	Masi	Renyi	Tsallis	Proposed
495	0.6202	0.2252	0.3656	0.3594	0.5283	0.3354	**0.9395**
502	0.9592	0.7742	0.5099	0.6296	0.6011	0.5469	**0.9785**
507	0.8827	0.7397	0.3978	0.5758	0.5427	0.3599	**0.9879**
508	0.8756	0.1450	0.4317	0.8364	0.5552	0.2579	**0.9710**
509	0.7607	0.4653	0.4288	0.8885	0.5954	0.3023	**0.9953**
513	0.7000	0.2905	0.4646	**0.9915**	0.6211	0.4987	0.9899
514	0.9040	0.6283	0.4411	0.5175	0.5987	0.3067	**0.9934**
1816	**0.9309**	0.9124	0.3717	0.2389	0.3730	0.3023	0.9307
1985	0.8333	0.0706	0.4986	0.6814	0.6655	0.4582	**0.9330**
1987	0.8590	0.9670	0.7822	0.3461	0.7528	0.6875	**0.9775**

Compared with Otsu's method, often considered a reliable benchmark, the proposed method shows clear advantages in complex segmentation scenarios. For example, in Image 495, Otsu achieves a moderate score of 0.6202, whereas the proposed method achieves a significantly higher score of 0.9395. Similarly, while the Masi algorithm achieves a competitive score of 0.9915 on Image 513, it lacks consistency, dropping to 0.2389 on Image 1816.

4.2.3. Similarity Measures

To evaluate the spatial overlap between segmentation results and ground truth, we used two widely accepted similarity metrics: the Dice similarity coefficient (DSC) and the Jaccard index (Intersection over Union: IoU). Higher values in both metrics indicate a stronger correlation between the segmented region and the reference image.

Table 4 summarizes the performance using the Dice metric. The proposed method demonstrated superior segmentation capability. It achieves the highest Dice scores across all ten test images. The scores for the proposed method range from 0.8628 (Image 1985) to 0.9488 (Image 507). It exhibits high consistency across image complexities. Compared with

the second-best-performing algorithm, the proposed approach showed significant improvements. For example, in Image 509, the proposed method achieved a Dice score of 0.9391, whereas Otsu's method dropped to 0.6900. This indicates a substantial variance in stability. Furthermore, traditional entropy-based methods, such as Shannon and Kapur, often fail to capture the region of interest effectively. They yield extremely low Dice scores (e.g., Kapur scored 0.0698 on Image 509). This significant performance gap clearly demonstrates the superiority of the proposed method over traditional thresholding algorithms.

Table 4. Quantitative evaluation of segmentation performance using the Dice metric. *Note: The best score in each row is highlighted in green bold, while the second-best score is highlighted in blue.*

Image No.	Otsu	Shannon	Kapur	Masi	Renyi	Tsallis	Proposed
495	0.6377	0.1318	0.2155	0.5213	0.5399	0.1755	**0.8920**
502	0.8773	0.6801	0.1789	0.3852	0.4691	0.3447	**0.9239**
507	0.9201	0.5522	0.1897	0.2510	0.5427	0.4067	**0.9488**
508	0.8806	0.2367	0.1360	0.3404	0.4460	0.0970	**0.9422**
509	0.6900	0.0778	0.0698	0.8297	0.3722	0.3342	**0.9391**
513	0.5526	0.3857	0.1162	0.3253	0.4293	0.3569	**0.9182**
514	0.8577	0.5603	0.1640	0.6858	0.4969	0.4206	**0.9262**
1816	0.8813	0.5915	0.1336	0.1698	0.4367	0.3298	**0.9135**
1985	0.7517	0.2610	0.4150	0.4168	0.5189	0.4613	**0.8628**
1987	0.7941	0.5828	0.6463	0.2929	0.5456	0.6305	**0.8898**

This superiority is also clearly reflected in the Jaccard index scores shown in Table 5. The proposed method consistently achieved the highest similarity indices. This indicates a more precise overlap with the ground truth. The proposed algorithm achieved Jaccard indices ranging from 0.7853 to 0.9064, consistently outperforming all six comparative algorithms. The performance gap was evident in challenging images such as Image 495. The proposed method recorded a Jaccard index of 0.8108, while the closest competitor, Otsu, achieved 0.5420, and Shannon dropped to 0.0791. This significant margin confirms that the proposed method yields segmentation results that are structurally closer to the ground truth. It minimizes both false positives and false negatives more effectively than the standard state-of-the-art methods evaluated.

Table 5. Quantitative evaluation of segmentation performance using the Jaccard metric. *Note: The best score in each row is highlighted in green bold, while the second-best score is highlighted in blue.*

Image No.	Otsu	Shannon	Kapur	Masi	Renyi	Tsallis	Proposed
495	0.5420	0.0791	0.1457	0.3794	0.4158	0.1032	**0.8108**
502	0.7893	0.5812	0.1070	0.3006	0.3463	0.2651	**0.8635**
507	0.8553	0.4873	0.1192	0.1613	0.4144	0.3480	**0.9064**
508	0.7946	0.1454	0.0769	0.2637	0.3272	0.0567	**0.8947**
509	0.6414	0.0440	0.0368	0.7310	0.2751	0.3023	**0.8881**
513	0.4421	0.3284	0.0643	0.3177	0.3198	0.3130	**0.8523**
514	0.7628	0.4937	0.0983	0.5836	0.3665	0.3458	**0.8663**
1816	0.8064	0.5413	0.0791	0.0980	0.3254	0.2476	**0.8472**
1985	0.6343	0.2145	0.3083	0.3586	0.3946	0.3807	**0.7853**
1987	0.6989	0.5228	0.5298	0.2270	0.4106	0.4883	**0.8071**

4.2.4. Pixel Classification Accuracy

This measures the ratio of correctly classified pixels (both foreground and background) to the total number of pixels and is presented in Table 6. A higher accuracy value indicates more precise segmentation, with values closer to 1.0 indicating near-perfect segmentation.

Table 6. Quantitative evaluation of segmentation performance using the accuracy metric. *Note: The best score in each row is highlighted in green bold, while the second-best score is highlighted in blue.*

Image No.	Otsu	Shannon	Kapur	Masi	Renyi	Tsallis	Proposed
495	0.6927	0.4173	0.3674	0.6017	0.6028	0.4380	**0.9550**
502	0.9615	0.8586	0.3607	0.4566	0.6272	0.4372	**0.9711**
507	0.9684	0.9010	0.3751	0.4126	0.6752	0.4546	**0.9775**
508	0.9608	0.4080	0.3506	0.7181	0.6410	0.4518	**0.9771**
509	0.9321	0.4415	0.3310	0.9666	0.6161	0.8745	**0.9733**
513	0.8029	0.8705	0.3302	0.8978	0.6232	0.8755	**0.9677**
514	0.9497	0.9136	0.3625	0.6724	0.6376	0.8450	**0.9777**
1816	0.9693	0.9569	0.3451	0.5325	0.6224	0.6467	**0.9838**
1985	0.9335	0.8103	0.7024	0.5398	0.7593	0.8584	**0.9476**
1987	0.9246	0.9091	0.7145	0.6093	0.6870	0.7910	**0.9554**

The quantitative results show that the proposed method consistently achieved the highest accuracy across all ten benchmark images, outperforming all six comparison algorithms. It exhibited strong stability, maintaining accuracy above 0.94 for each test image. The Otsu algorithm often ranked second (shown in blue), especially for images like 507 (0.9684) and 1816 (0.9693). However, its performance dropped significantly on lower-contrast images like 495, achieving only 0.6927, compared to 0.9550 for the proposed method. The entropy-based methods showed significant instability. For instance, on Image 508, Shannon and Kapur yielded very low accuracy scores of 0.4080 and 0.3506, respectively, failing to correctly classify most pixels. In contrast, the proposed method maintained a robust accuracy of 0.9771 on the same image. While Masi performed competitively on specific images (e.g., scoring 0.9666 on Image 509), it lacked consistency, dropping to 0.4126 on Image 507.

The significant performance gap, particularly on challenging images such as 495 and 508, indicates that the proposed method is far more robust to variations in image contrast and noise than standard thresholding techniques. While Otsu remains a reliable alternative in some scenarios, the proposed algorithm consistently delivers the most accurate pixel-wise segmentation.

4.2.5. Precision and Recall

The segmentation quality was further analyzed using precision and recall metrics to evaluate the trade-off between false positives and false negatives. These metrics are critical for understanding whether an algorithm is over-segmenting (high recall, low precision) or under-segmenting (high precision, low recall).

Table 7 presents the precision values, which measure the proportion of true positive pixels among all pixels classified as part of the object. The proposed method demonstrated the highest precision across all ten test images, consistently achieving values above 0.87. Notably, for Image 507, the proposed method achieved a precision of 0.9569. It significantly outperformed the second-best method, Otsu, which scored 0.8909. In complex images such as Image 513, traditional methods, such as Otsu and Masi, struggled. The results yielded precision scores of 0.4970 and 0.3212, respectively. In contrast, the proposed method maintained a high precision of 0.9422. This indicates a strong capability to suppress background noise and false positives.

Table 7. Quantitative evaluation of segmentation performance using the precision metric. *Note: The best score in each row is highlighted in green bold, while the second-best score is highlighted in blue.*

Image No.	Otsu	Shannon	Kapur	Masi	Renyi	Tsallis	Proposed
495	0.6406	0.7348	0.4756	0.7245	0.5477	0.7360	**0.9355**
502	0.8439	0.6004	0.4407	0.7123	0.4654	0.6054	**0.9120**
507	0.8909	0.8228	0.4497	0.4755	0.5190	0.7122	**0.9569**
508	0.8481	0.4721	0.4076	0.5748	0.4412	0.3890	**0.9406**
509	0.6683	0.3785	0.3700	0.8066	0.3962	0.6796	**0.9407**
513	0.4970	0.6484	0.3984	0.3212	0.4264	0.4937	**0.9422**
514	0.8527	0.9145	0.4309	0.5894	0.4830	0.6674	**0.9182**
1816	0.8943	0.5570	0.3999	0.7175	0.4429	0.7091	**0.9328**
1985	0.7050	0.2145	0.6643	0.3694	0.4774	0.6967	**0.9185**
1987	0.7664	0.5902	0.5871	0.5329	0.5116	0.7962	**0.8754**

Table 8 details the recall values, representing the ability of the algorithm to capture the complete region of interest (ROI). The proposed method maintained robust recall rates, ranging from 0.8346 to 0.9443. Specific cases show that traditional algorithms perform better than others on recall. The Masi algorithm recorded a value of 0.9738 for Image 514. The proposed method scored lower at 0.9358. Otsu's method also performed well on Image 509. It attained a recall of 0.9610. The proposed method scored 0.9381 for that same image.

Table 8. Quantitative evaluation of segmentation performance using the recall metric. *Note: The best score in each row is highlighted in green bold, while the second-best score is highlighted in blue.*

Image No.	Otsu	Shannon	Kapur	Masi	Renyi	Tsallis	Proposed
495	0.6870	0.3394	0.3881	0.6530	0.6361	0.3626	**0.8626**
502	0.9207	**0.9609**	0.4614	0.5723	0.6638	0.5877	0.9366
507	**0.9541**	0.6334	0.4294	0.4571	0.7139	0.6308	0.9418
508	0.9212	0.6624	0.4385	0.3313	0.6928	0.3277	**0.9443**
509	**0.9610**	0.2092	0.4145	0.8980	0.6750	0.3483	0.9381
513	0.7591	0.3783	0.4165	0.3296	0.6828	0.3606	**0.8976**
514	0.8826	0.5467	0.4315	0.9738	0.6826	0.4050	**0.9358**
1816	0.8741	0.6399	0.4113	0.3598	0.6255	0.4720	**0.9079**
1985	**0.8823**	0.3333	0.5748	0.7282	0.8132	0.4693	0.8346
1987	**0.9146**	0.5786	0.8694	0.3531	0.7364	0.6726	0.9140

However, this higher recall in competing methods is misleading when viewed in isolation. By comparing these cases with Table 7, Masi's high recall on Image 514 is accompanied by a very low precision of 0.5894, and Otsu's high recall on Image 509 corresponds to a precision of 0.6683. Traditional methods produced higher recall scores. This result arises from significant over-segmentation. Consequently, the algorithms identified many background pixels as part of the object.

4.2.6. Statistical Distribution of Segmentation Performance

Figure 6 presents box plots for all six performance metrics. It provides a visual summary of the statistical distribution and stability of each segmentation method.

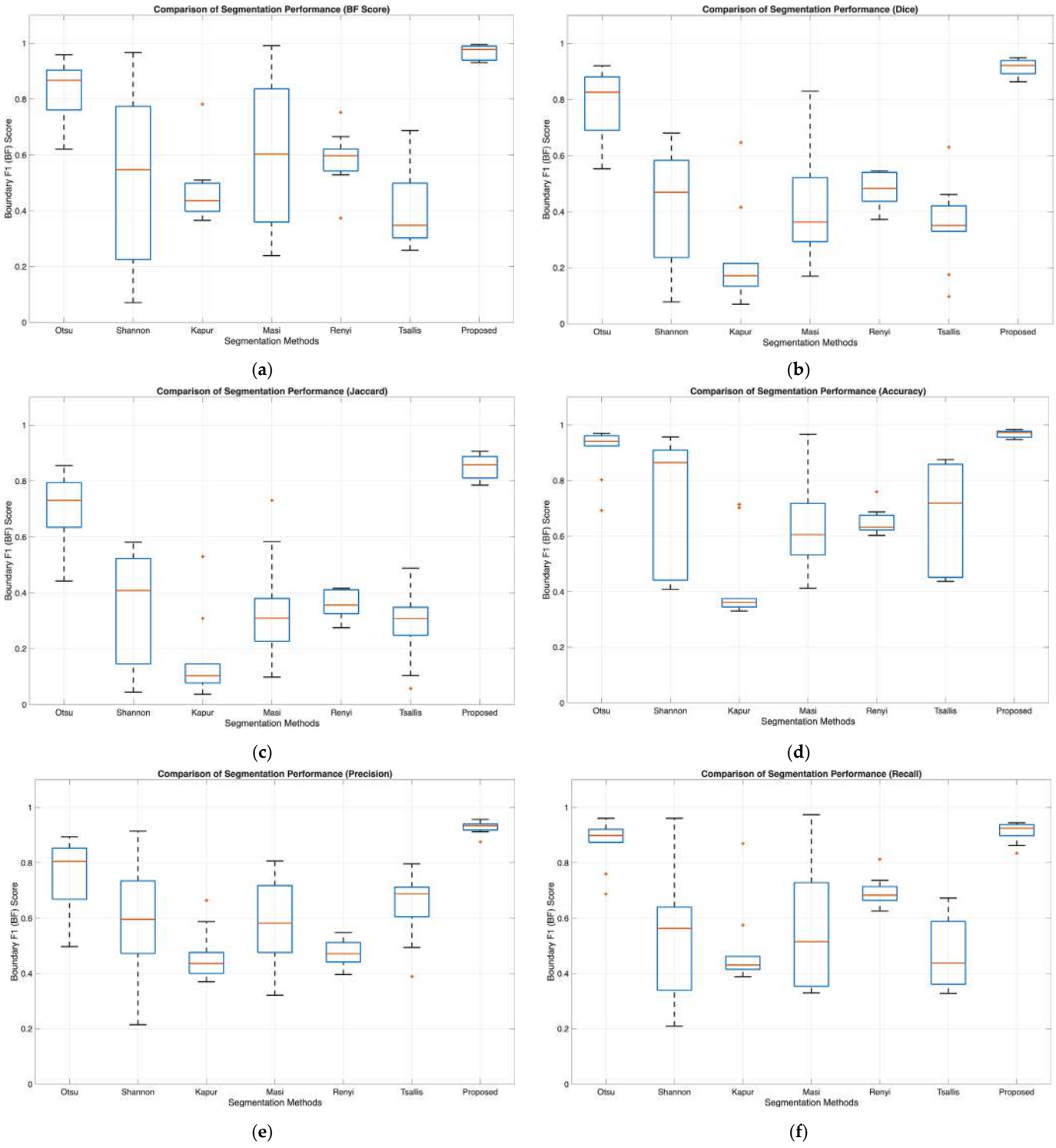

Figure 6. Statistical distribution of segmentation performance for the proposed method compared to state-of-the-art entropy-based algorithms: (**a**) BF score metric, (**b**) Dice metric, (**c**) Jaccard, (**d**) accuracy metric, (**e**) precision metric, and (**f**) recall metric. In each plot, the central red line indicates the median; the blue box represents the interquartile range (25th to 75th percentiles); the whiskers extend to the minimum and maximum values within 1.5 times the interquartile range; and the orange symbols (+) represent individual outliers.

To facilitate a clear understanding of the stability and variability of the segmentation algorithms, the results are presented using box-and-whisker plots. These plots provide a standardized summary of the data distribution based on a five-number summary: the

minimum, the first quartile (Q_1), the median, the third quartile (Q_3), and the maximum. The key components of the chart are interpreted as follows:

- The Box (Interquartile Range): The rectangular body of the plot represents the Interquartile Range (IQR), spanning from Q_1 (25th percentile) to Q_3 (75th percentile). This area contains the middle 50% of the data. A shorter, more compact box indicates high consistency and low variance in the algorithm's performance across different images. Conversely, a taller box suggests unstable performance, with accuracy fluctuating significantly across input images.
- The Median (Red Line): The line dividing the box represents the median score. This value indicates the typical performance level of the method, offering a robust measure of central tendency that is less influenced by outliers than the arithmetic mean.
- The Whiskers: The vertical lines extending from the box indicate the variability outside the upper and lower quartiles. They typically extend to the minimum and maximum data points that fall within 1.5 × IQR. Long whiskers extending downward indicate that an algorithm is prone to occasional poor performance or failure cases.
- Outliers (Red Dot): Individual points plotted beyond the whiskers represent outliers—extreme values that deviate significantly from the rest of the dataset. In this study, outliers at the bottom of the chart highlight specific images where an algorithm failed to achieve acceptable segmentation.

A comparative analysis of these plots reveals distinct characteristics of the proposed algorithm's reliability relative to state-of-the-art entropy-based techniques. The proposed method achieves the highest median across all six performance metrics. As indicated by the median line within the boxes, the proposed algorithm consistently centers on the 0.93–0.98 range for accuracy-related metrics. In contrast, traditional entropy-based methods such as Shannon and Kapur exhibit significantly lower medians, often below 0.5 for metrics such as the Jaccard index. This reflects their general inability to accurately segment complex Arctic imagery.

The compactness of the box determines the consistency of an algorithm. The proposed method introduces the most compact box plots. It indicates minimal variance in performance across the dataset. This tightness confirms that the algorithm is highly robust, delivering predictable results regardless of image characteristics. On the other hand, Masi and Renyi show vertically distributed boxes with wide whiskers. For instance, while Masi achieves a high BF score of 0.9915 on Image 513, it drops to 0.2389 on Image 1816. This large spread in the box plot visually highlights the unpredictability of these methods, which fluctuate heavily depending on image contrast.

The whiskers of the box plots for Otsu, Shannon, and Kapur extend significantly downward. This pattern indicates instances of severe performance failure. Specifically, Shannon and Kapur display extreme lows. Their Dice scores drop to 0.0778 and 0.0698, respectively. In contrast, the proposed method demonstrates short lower whiskers. Its minimum Dice score remains robust at 0.8628. This absence of low-value outliers underscores the reliability of the proposed method. The segmentation quality remains consistent for practical analysis.

4.2.7. Holistic Performance Analysis

To evaluate the overall effectiveness and balance of each segmentation algorithm, we computed the average scores across all test images for six key metrics: boundary F1 (BF) score, Dice similarity coefficient, Jaccard index, accuracy, precision, and recall. These averages are visualized in the radar chart illustrated in Figure 7.

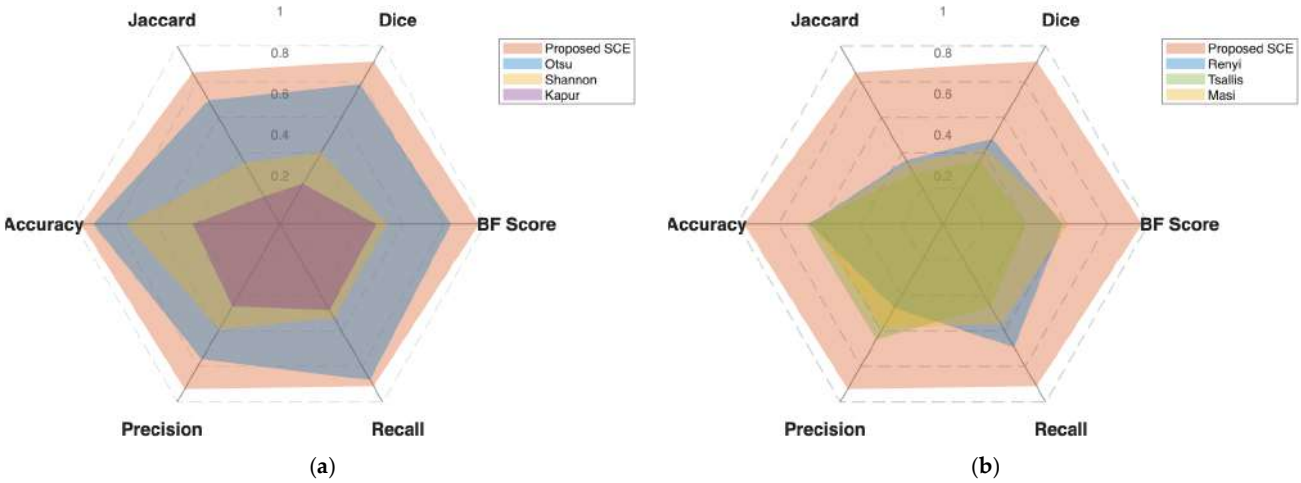

Figure 7. Average performance comparison of the proposed SCE method across the HOTRAX dataset: (**a**) comparison with Otsu and non-parametric entropy models, and (**b**) comparison with parametric-based entropy models.

To assist in analyzing the algorithms' overall efficacy, the results are presented in a radar chart (also known as a spider chart). This visualization technique displays multivariate data on a two-dimensional chart, with three or more quantitative variables represented on axes that share a common origin. The key components of the chart are interpreted as follows:

- Axes and Scales: Each spoke represents one of the six performance metrics. The scale for each axis ranges from 0 (center) to 1 (outer edge), where 1.0 represents perfect performance.
- Polygon Area: The data points for each algorithm are connected to form a polygon. A larger polygon area indicates superior overall performance across all metrics. A smaller polygon suggests poor performance or failure in specific categories.
- Shape and Symmetry: The shape of the polygon reveals the balance of the algorithm. A regular, symmetric polygon indicates a well-balanced method that performs consistently across all metrics (e.g., high precision and recall). An irregular or "dented" shape highlights trade-offs, such as an algorithm that achieves high recall at the expense of precision.

Figure 7a compares the proposed symmetric cross-entropy (SCE) method with the variance-based Otsu method and traditional non-parametric entropies such as Shannon and Kapur. The proposed method produces the outermost polygon (shown in orange) and outperforms all other algorithms, achieving the highest average scores across all metrics. The polygon's symmetry indicates a robust balance between precision (0.9273) and recall (0.9113). This confirms that the SCE approach effectively delineates ice features without the trade-offs typical of other methods.

In contrast, the Otsu method exhibits a characteristic dented shape. While it maintains a competitive recall and accuracy, its polygon retracts significantly along the Jaccard and BF score axes. This visual discrepancy highlights Otsu's tendency toward oversegmentation; while it successfully detects ice pixels, it fails to accurately trace morphological boundaries, resulting in a lower boundary F1 score of 0.8326 compared to 0.9697 for the proposed method.

Furthermore, the non-parametric entropy-based methods, such as Shannon and Kapur, appear as collapsed polygons near the center of the chart. Their minimal area reflects a systemic failure to adapt to the multimodal histograms of Arctic scenes, where pixel intensities for melt ponds and thin ice overlap significantly.

Figure 7b benchmarks the proposed method against parametric entropy models like Renyi, Tsallis, and Masi. While these parametric models generally outperform the non-parametric ones by covering a larger area of the chart, they still lack the structural fidelity of the proposed method.

The parametric models cluster in the middle range. It is indicated by the overlapping blue, green, and yellow polygons. They exhibit weakness in the shape-based metrics—BF score and Jaccard index—where their polygons retract inward. For instance, Tsallis entropy shows a notable imbalance, often sacrificing precision for moderate recall, which manifests as an irregular shape in the chart.

The proposed SCE method envelops these parametric models entirely. This visualization provides strong evidence that the symmetric cross-entropy formulation yields a more effective objective function for Arctic image segmentation than simply adding tunable parameters to standard entropy measures. By maximizing the divergence between the original and smoothed histograms, the proposed method achieves holistic superiority, balancing pixel-level accuracy with morphological precision.

4.2.8. Class-Specific Segmentation Performance

To further understand the strengths and limitations of the proposed symmetric cross-entropy (SCE) method, a class-specific performance evaluation was conducted. While holistic metrics provide an overview of algorithmic stability, analyzing performance across individual ice features highlights how physical and spectral properties influence segmentation. Table 9 presents the average accuracy, precision, and recall scores achieved by the proposed method, broken down by the three primary target classes: open water, ice/snow, and melt ponds (including slush).

Table 9. Average class-specific segmentation performance of the proposed SCE method across the HOTRAX dataset.

Class	Accuracy	Precision	Recall	Dice	Jaccard	F1
Open Water	0.9388	0.8819	0.6274	0.7089	0.6206	0.7089
Ice/Snow	0.9486	0.9398	0.9990	0.9654	0.9388	0.9654
Melt Ponds	0.9902	0.9455	0.9029	0.8935	0.8443	0.8935

The class-specific evaluation detailed in Table 9 reveals varying degrees of segmentation performance that strongly correlate with the physical and spectral characteristics of each Arctic feature. By analyzing the accuracy, precision, recall, and F1 scores across the three target classes, we can better understand the specific behavioral strengths and limitations of the proposed symmetric cross-entropy (SCE) method.

Melt ponds achieved the highest overall pixel accuracy (0.9902) alongside a strong precision of 0.9455. Historically, melt ponds have been among the most challenging features to segment because they are semi-transparent, transitional zones (often containing slush) whose intensity varies with water depth and the brightness of the underlying ice. The high precision and accuracy indicate that the proposed SCE method, utilizing local-minima histogram smoothing, successfully isolates these complex regions without generating the severe over-segmentation or false-positive noise typical of variance-based methods like Otsu. The exceptionally high accuracy metric also reflects the algorithm's strong true negative classification rate for this feature, as melt ponds typically occupy a smaller total pixel area than vast ice floes.

The solid ice and snow regions demonstrate outstanding structural capture, evidenced by a near-perfect recall score of 0.9990 and the highest overall F1 score (0.9654). This indicates that the algorithm successfully identifies and retains almost the entirety of the

solid ice floes without suffering from the under-segmentation failures seen in traditional entropy models like Shannon or Tsallis. There is a slight drop in precision (0.9398) relative to recall; this implies that a small fraction of boundary pixels from other classes (such as bright slush or reflections on water) are occasionally grouped into the dominant ice class. However, the high F1 score confirms that the geometric fidelity of the ice floes remains highly intact.

Open water proved to be the most challenging class to segment comprehensively. While it maintains a respectable pixel accuracy (0.9388) and precision (0.8819), its recall drops significantly to 0.6274. This indicates a higher rate of false negatives. Physically, this occurs because the spectral intensity of deep, dark open-water channels occasionally overlaps with the darkest regions of deep melt ponds or heavily shadowed ice edges. Consequently, the intensity-based thresholding mechanism occasionally misses open-water pixels, blending them into adjacent transitional zones. Despite this challenge, the high precision (0.8819) demonstrates that when the algorithm classifies a region as open water, it is highly likely to be correct, prioritizing the suppression of false positives over exhaustive detection.

4.2.9. Computational Cost and Efficiency Analysis

Computational efficiency is essential for the practical deployment of segmentation algorithms in large-scale Arctic monitoring. To evaluate this, we recorded the average execution time per image (in seconds) for the proposed method and comparative algorithms.

To unify classification performance and computational efficiency into a single quantitative metric, we introduce the Boundary F1-Efficiency Index (BFEI). Because standard pixel-wise accuracy can be skewed by class imbalance, we utilize the boundary F1 (BF) score to prioritize geometric fidelity. The index is defined as

$$BFEI = BF \times \ln(T), \tag{12}$$

where T represents the processing throughput (calculated as images per second). The logarithmic term ensures that significant increases in speed contribute meaningfully to the efficiency score without overshadowing the importance of segmentation accuracy.

As demonstrated in Table 10, the proposed symmetric cross-entropy (SCE) method is highly efficient, requiring approximately 1.87 s per image. Despite the mathematical complexity of the cross-entropy formulation, restricting the optimal threshold search space to the local minima of the smoothed histogram allows the algorithm to operate at speeds comparable to the simple variance-based Otsu method. Consequently, the proposed method achieves the highest *BFEI*, demonstrating superior boundary delineation without introducing a prohibitive computational bottleneck.

Table 10. Computational cost and efficiency evaluation. *Note: The best score in each row is highlighted in green bold, and average BF scores for comparative algorithms are aggregated from* Table 3.

Method	Throughput (t, Image/Sec.)	Average BF Score	BFEI
Otsu	**1.8646**	0.8326	0.2253
Shannon	2.0052	0.5218	0.1577
Renyi	1.9703	0.5834	0.1718
Masi	2.0169	0.6065	0.1848
Kapur	2.1060	0.4692	0.1518
Tsallis	1.9312	0.4056	0.1159
Proposed	1.8709	**0.9697**	**0.2638**

4.3. Qualitative Evaluation

To complement the quantitative analysis, we visually inspected the segmentation results to assess how well each algorithm handled the complex features of Arctic sea ice, including snow, melt ponds, and open water. Figure 8 illustrates the segmentation outputs from the HOTRAX dataset, comparing the proposed method against standard algorithms and the ground truth.

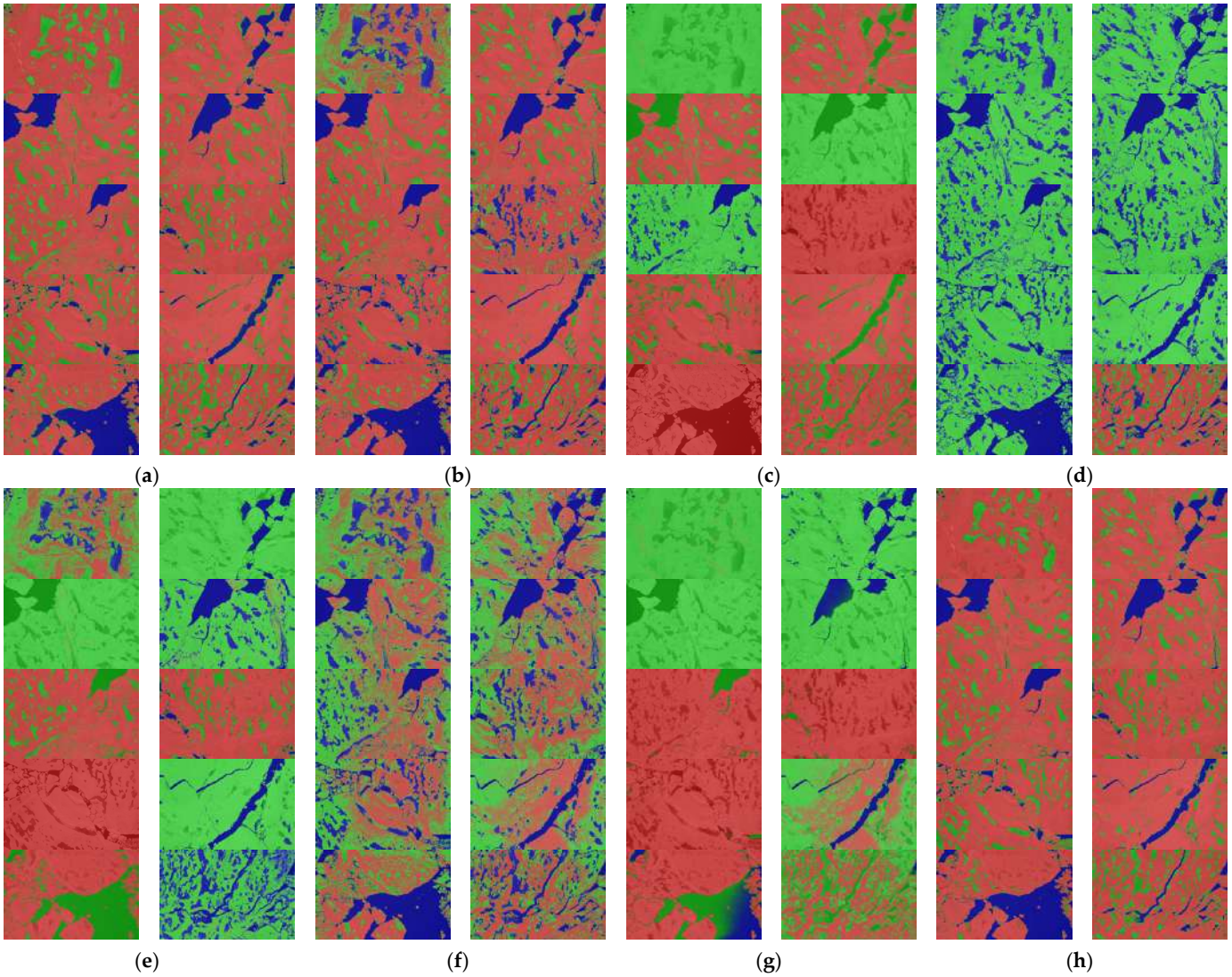

Figure 8. Visual comparison of segmentation results for example images from the HOTRAX dataset: (**a**) ground truth, (**b**) Otsu, (**c**) Shannon, (**d**) Kapur, (**e**) Masi, (**f**) Renyi, (**g**) Tsallis, and (**h**) proposed method. *The color key indicates distinct regions:* ■ *open water,* ■ *snow,* ■ *melt ponds.*

4.3.1. Analysis of Variance-Based Method

While Otsu's method, as shown in Figure 8b, generally outperformed the entropy-based techniques, the qualitative evaluation highlights a distinct tendency toward over-segmentation. Although Otsu's method successfully captures the general ice area, it lacks stability in tracing irregular boundaries. Visually, this manifests as the incorrect labeling of open water and dark slush as sea ice. This observation aligns with the precision–recall analysis, where Otsu's method frequently achieved competitive recall but significantly lower precision, indicating a high rate of false positives. Consequently, while it detects ice, it fails to preserve the morphological details needed for accurate ice-floe analysis.

4.3.2. Analysis of Entropy-Based Methods

The visual inspection reveals severe limitations in traditional entropy-based methods (Shannon, Kapur, Tsallis, Renyi, and Masi) when applied to heterogeneous ice imagery. As seen in Figure 8c,d,g, methods such as Shannon and Tsallis failed significantly to define ice edges. The resulting segmentation maps exhibit substantial under-segmentation, with large sections of the ice structure missing or treated as background. This visual failure corroborates the quantitative results, which show that Shannon and Kapur yielded negligible Jaccard scores (e.g., 0.0440 and 0.0368, respectively) on complex images. This performance collapse is likely due to the inability of global entropy calculations to adequately handle the multimodal histograms typical of melting ice surfaces.

4.3.3. Extended Visual Analysis of Complex Ice Topologies

Figure 9 presents the segmentation results for Image 495, a scene characterized by large regions of snow interspersed with melt ponds and a narrow channel of open water. As observed in Figure 9c,g, traditional entropy models suffered from severe under-segmentation. These algorithms failed to distinguish between the spectral signatures of snow and melt ponds. They merged the regions into a single class. This results in a segmentation map that completely loses the topographical structure of the ice surface. While Otsu's method, as illustrated in Figure 9b, successfully identified the presence of snow, it introduced significant salt-and-pepper noise.

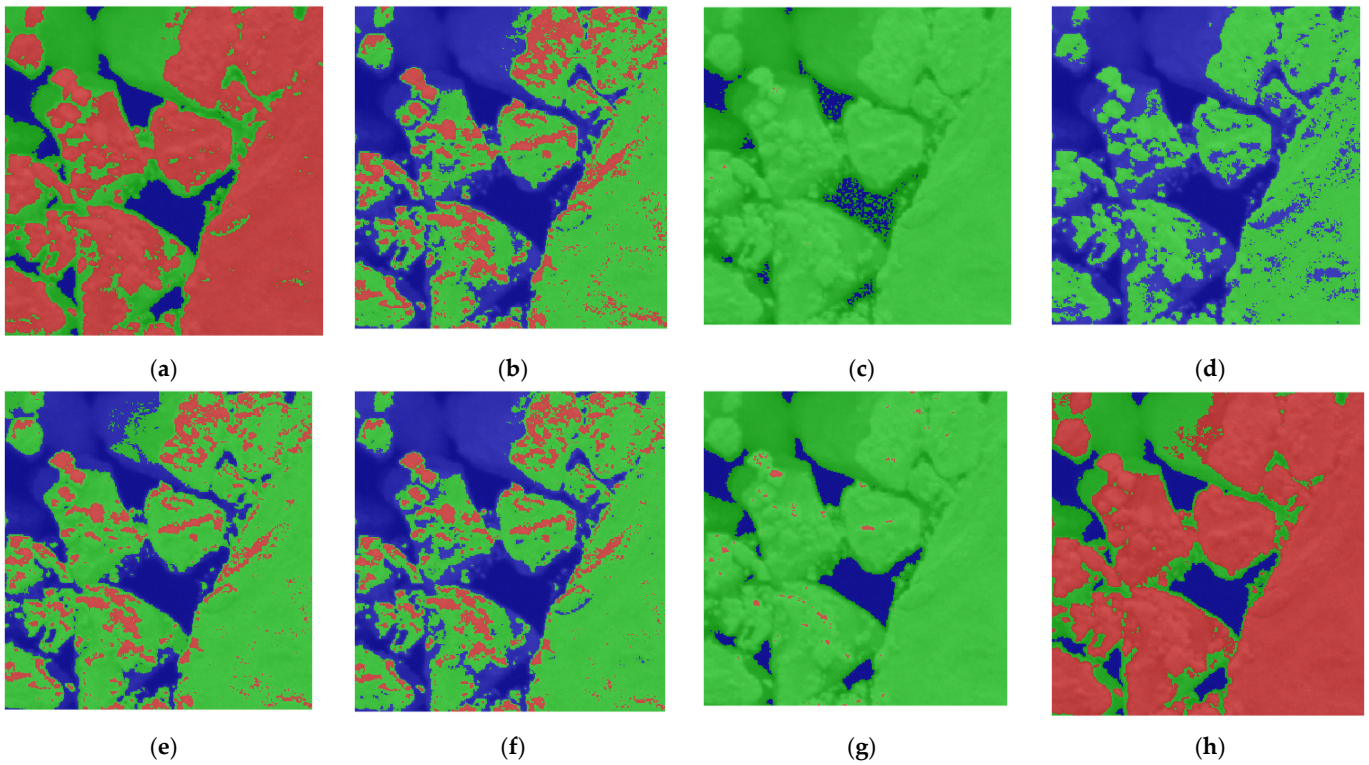

Figure 9. Extracted region comparison of segmentation results for Image 1985 from the HOTRAX dataset: (**a**) ground truth, (**b**) Otsu, (**c**) Shannon, (**d**) Kapur, (**e**) Masi, (**f**) Renyi, (**g**) Tsallis, and (**h**) proposed method. *The color key indicates distinct regions:* ■ *open water,* ■ *snow,* ■ *melt ponds.*

The snow regions are heavily fragmented by incorrect pixels. This indicates that local brightness variations were misclassified as melt ponds. In contrast, the proposed method, as demonstrated in Figure 9h, achieved a result nearly identical to the ground truth, as shown in Figure 9a. It successfully separated the snow from the melt ponds. It defined these features with sharp and cohesive boundaries. Unlike Shannon and Tsallis

entropies, the proposed method prevented under-segmentation artifacts. It also avoided the salt-and-pepper noise characteristic of Otsu's technique.

Figure 10 illustrates a fragmented ice field where the challenge lies in maintaining the integrity of individual ice floes against a dark water background. The instability of parametric entropies is evident in Figure 10e, which produced a great segmentation failure. The algorithm misclassified almost the entire ice surface as melt ponds. Consequently, the snow layer was lost entirely. Figure 10g illustrates a similar failure with Tsallis entropy. This method produced large, amorphous regions. These shapes do not represent physical features. Otsu, as shown in Figure 10b, and Renyi, as shown in Figure 10f, exhibit a tendency to over-segment natural texture. These algorithms interpreted the rough surface of the ice floes as disjointed classes. This misinterpretation resulted in a noisy, speckled appearance. Consequently, regions of solid ice were incorrectly labeled as melt ponds. Shannon exhibits a critical failure in class separation. As shown in Figure 10c, the algorithm fails to distinguish dark open-water channels from the ice surface. Consequently, it merges the water and snow classes into a single dominant region. This results in severe under-segmentation where the topological structure of the ice field is completely lost. While Kapur's method, as shown in Figure 10d, outperforms Shannon at identifying water channels, it struggles with boundary precision.

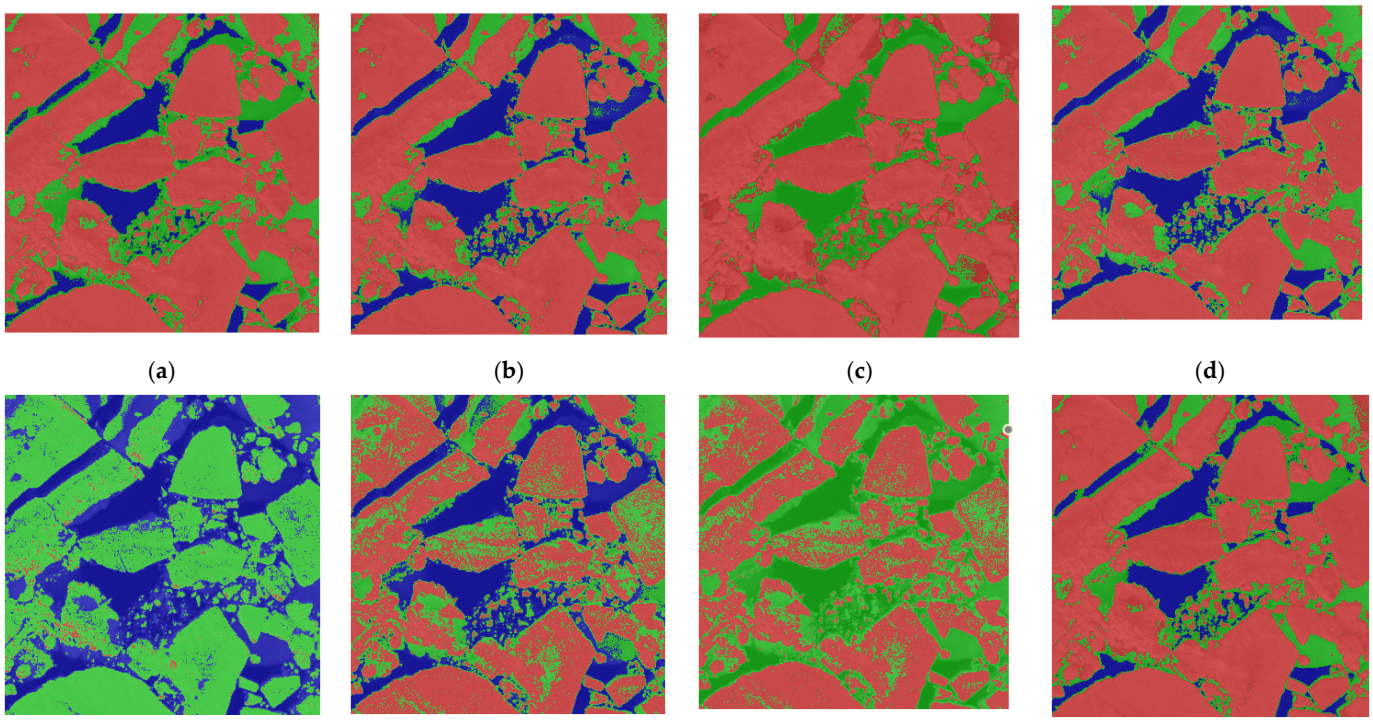

Figure 10. Extracted region comparison of segmentation results for Image 1987 from the HOTRAX dataset: (**a**) ground truth, (**b**) Otsu, (**c**) Shannon, (**d**) Kapur, (**e**) Masi, (**f**) Renyi, (**g**) Tsallis, and (**h**) proposed method. *The color key indicates distinct regions:* ■ *open water,* ■ *snow,* ■ *melt ponds.*

The segmentation introduces significant noise along the edges of the ice floes. The melted pond regions are frequently exaggerated or misclassified within the solid ice. This inconsistency aligns with the lower Jaccard scores observed in the quantitative analysis. The proposed method, as shown in Figure 10h, demonstrates superior morphological fidelity. It preserved the solid structure of the ice floes. The algorithm also correctly identified the true melt ponds located at the floe edges. The proposed method utilizes the local minima of the smoothed histogram. This approach effectively ignored intra-class texture variance.

Conversely, this variance confused the Otsu and Renyi methods. The results demonstrate a topologically accurate segmentation map.

4.3.4. Performance of the Proposed Method

The qualitative evaluation across Figures 8 and 9 demonstrates the proposed symmetric cross-entropy (SCE) method's superior capability to preserve geometric fidelity and structural integrity compared to state-of-the-art techniques. While variance-based algorithms like Otsu and texture-sensitive entropies like Rényi frequently yield to over-segmentation, they manifest as salt-and-pepper noise, with rough ice textures misclassified as melt ponds. The proposed method uses local-minimum smoothing to effectively ignore intra-class variance. It results in clean and topologically accurate segmentation maps. On the other hand, traditional entropy models such as Shannon and Tsallis fail to distinguish spectrally similar classes. They lead to the merging of snow and melt ponds; the proposed method maintains sharp, cohesive boundaries that closely mirror the ground truth. In addition, the proposed algorithm exhibits exceptional stability across diverse ice topologies. It avoids the catastrophic failures observed in parametric models like Masi and achieves a robust balance between precision and recall that is critical for operational Arctic monitoring.

5. Conclusions

This paper introduced the symmetric cross-entropy (SCE) multi-level thresholding algorithm, a novel approach designed to address the significant challenges of segmenting low-contrast Arctic imagery. By combining a hybrid cross-entropy maximization criterion with local-minima analysis and histogram smoothing, the proposed method effectively categorizes complex scenes into distinct classes, such as ice, melt ponds, and open water.

Comprehensive quantitative evaluations on the HOTRAX dataset demonstrated that the SCE method consistently outperforms state-of-the-art entropy-based methods, including Shanon, Kapur, Renyi, Tsallis, and Masi. Unlike traditional methods, which exhibited severe failures in complex scenes, the proposed algorithm maintained exceptional stability. It achieves accuracy rates between 94.76% and 98.38%. Notably, the method achieved a robust balance between precision and recall, avoiding the over-segmentation behavior observed with variance-based methods such as Otsu. While Otsu's method frequently compromised precision to maximize recall, the proposed approach maintained both metrics above 0.83 significantly. It is evident that the proposed technique can reduce false positives.

Furthermore, the algorithm demonstrated superior capability in preserving the geometric fidelity of ice features. It yields boundary F1 (BF) scores ranging from 0.9307 to 0.9953. Statistical analysis of region-overlap metrics confirmed this spatial accuracy, with Jaccard scores consistently ranging from 0.7853 to 0.9064. This indicates reliable identification of ice features without misclassifying submerged ice or open water. These advancements provide high-quality, automated data for ice feature recognition, which is important for operational planning, risk assessment, and predictive modeling. By addressing the limitations of standard global entropy calculations in multimodal histograms, this method represents a significant step forward in Arctic sea research and offshore engineering applications.

Despite the robust performance of the proposed symmetric cross-entropy (SCE) method, it is important to acknowledge the inherent limitations of 1D intensity-based thresholding. Because the algorithm relies primarily on global histogram distributions, it lacks explicit spatial contextual awareness. In highly complex Arctic scenes, distinct physical features, such as shadowed ice edges and deep open water, may exhibit nearly identical intensity values, potentially leading to pixel-wise misclassification in spectrally ambiguous zones.

While the proposed local-minima smoothing effectively mitigates high-frequency noise and preserves topological boundaries better than standard variance-based methods, future iterations of this work will explore integrating spatial information. Extending the SCE framework to utilize 2D histograms (which incorporate local neighborhood averaging) or coupling the thresholding outputs with Markov Random Field (MRF) refinement or Convolutional Neural Networks (CNNs) could further enhance classification robustness while maintaining the high boundary precision demonstrated in this study.

Author Contributions: Conceptualization, S.S.A.; methodology. T.T.; software, T.T.; formal analysis, T.T., S.S.C., K.D., A.A.F. and S.S.A., resources, T.T.; writing—original draft, T.T.; writing—review and editing, T.T. and S.S.A., supervision, T.T., S.S.C., K.D., A.A.F. and S.S.A. All authors have read and agreed to the published version of the manuscript.

Funding: This research received no external funding.

Institutional Review Board Statement: Not applicable.

Data Availability Statement: The data presented in this study are available on request from the corresponding author.

Acknowledgments: The authors would like to express their gratitude to Rajamangala University of Technology Phra Nakhon (RMUTP) for providing the MATLAB version 2025b software license used in this study.

Conflicts of Interest: The authors declare no conflicts of interest.

References

1. Andersson, T.; Agocs, F.; Hosking, S.; Pérez-Ortiz, M.; Paige, B.; Russell, C.; Elliott, A.; Law, S.; Wilkinson, J.; Askenov, Y.; et al. Deep Learning for Monthly Arctic Sea Ice Concentration Prediction. In Proceedings of the EGU General Assembly Conference Abstracts, Online, 1 May 2020; p. 15481.
2. Kohnert, K.; Juhls, B.; Muster, S.; Antonova, S.; Serafimovich, A.; Metzger, S.; Hartmann, J.; Sachs, T. Toward understanding the contribution of waterbodies to the methane emissions of a permafrost landscape on a regional scale-A case study from the Mackenzie Delta, Canada. *Glob. Change Biol.* **2018**, *24*, 3976–3989. [CrossRef]
3. Jiang, Z.; Von Ness, K.; Loisel, J.; Wang, Z. ArcticNet: A Deep Learning Solution to Classify Arctic Wetlands. *arXiv* **2019**, arXiv:1906.00133. [CrossRef]
4. Trongtirakul, T.; Agaian, S.; Oulefki, A.; Panetta, K. Method for Remote Sensing Oil Spill Applications Over Thermal and Polarimetric Imagery. *IEEE J. Ocean. Eng.* **2023**, *48*, 973–987. [CrossRef]
5. Kumar, A.; Jain, M.; Dev, S. Generative Augmentation for Sky/Cloud Image Segmentation. In Proceedings of the IGARSS 2023—2023 IEEE International Geoscience and Remote Sensing Symposium, Pasadena, CA, USA, 16–21 July 2023; pp. 7288–7291.
6. Liu, M. Momentum Contrast Learning for Aerial Image Segmentation and Precision Agriculture Analysis. In Proceedings of the 2022 International Conference on Image Processing, Computer Vision and Machine Learning (ICICML), Xi'an, China, 28–30 October 2022; pp. 31–34.
7. Zhang, P.; He, H.; Wang, Y.; Liu, Y.; Lin, H.; Guo, L.; Yang, W. 3D Urban Buildings Extraction Based on Airborne LiDAR and Photogrammetric Point Cloud Fusion According to U-Net Deep Learning Model Segmentation. *IEEE Access* **2022**, *10*, 20889–20897. [CrossRef]
8. Baur, A.; Landerer, S.; Schulze, D.; Praetorius, J.; Borchers, H.; Günther, O.; Holm, H. Semi-Automated Semantic Segmentation of Arctic Shorelines Using Very High-Resolution Airborne Imagery, Spectral Indices and Weakly Supervised Machine Learning Approaches. *Remote Sens.* **2021**, *13*, 4572.
9. Doherty, P.H.; Matthes, J.T.; French, J.R.; Duffy, J.A.; Hood, B.K.; Kane, D.L.; Fisher, J.A.D.; Pomeroy, J.W.; Hinzman, L.D.; Stieglitz, M.; et al. Arctic-COLORS (Coastal Land Ocean Interactions in the Arctic)—A NASA field campaign scoping study to examine land-ocean interactions in the Arctic. In Proceedings of the AGU Fall Meeting Abstracts, San Francisco, CA, USA, 1 December 2014; pp. B43B–0242.
10. National Academies of Sciences, Engineering, and Medicine; Division on Earth and Life Studies; Board on Science and Technology for Sustainable Development; Committee on the Decadal Survey for Earth Science and Applications from Space. *Thriving on Our Changing Planet: A Decadal Strategy for Earth Observation from Space*, Illustrated ed.; National Academies Press: Cambridge, MA, USA, 2018.

11. Farquharson, L.; Mann, D.; Swanson, D.; Jones, B.; Buzard, R.; Jordan, J. Temporal and spatial variability in coastline response to declining sea-ice in northwest Alaska. *Mar. Geol.* **2018**, *404*, 71–83. [CrossRef]
12. Marshall, G.J.; Dowdeswell, J.A.; Rees, W.G. The spatial and temporal effect of cloud cover on the acquisition of high quality landsat imagery in the European Arctic sector. *Remote Sens. Environ.* **1994**, *50*, 149–160. [CrossRef]
13. Rusin, J.; Doulgeris, A.P.; Scott, K.A.; Lavergne, T.; Taelman, C. High Resolution Sea Ice Concentration Using a Sentinel-1 U-Net Ice-Water Classifier. *IEEE J. Sel. Top. Appl. Earth Obs. Remote Sens.* **2025**, *18*, 9380–9395. [CrossRef]
14. Jiang, M.; Xu, L.; Clausi, D.A. Sea Ice–Water Classification of RADARSAT-2 Imagery Based on Residual Neural Networks (ResNet) with Regional Pooling. *Remote Sens.* **2022**, *14*, 3025. [CrossRef]
15. Chen, J.; Huang, W. GNSS-R Based Sea Ice Classification Using Track Normalized Observables. In Proceedings of the OCEANS 2025 Brest, Brest, France, 16–19 June 2025; pp. 1–4.
16. Yan, Q.; Huang, W. Sea Ice Remote Sensing Using GNSS-R: A Review. *Remote Sens.* **2019**, *11*, 2565. [CrossRef]
17. Li, W.; Karkamkar, V.; Liu, Y.; Amin, S.; Janowicz, K.; Witharana, C. Real-Time GeoAI for High-Resolution Mapping and Segmentation of Arctic Permafrost Features: The Case of Ice-Wedge Polygons. In Proceedings of the Proceedings of the 5th ACM SIGSPATIAL International Workshop on AI for Geographic Knowledge Discovery, Seattle, WA, USA, 1 November 2022; pp. 62–65.
18. Oulefki, A.; Amira, A.; Kurugollu, F.; Trongtirakul, T.; Agaian, S.; Mohammed, M.K.; Alshoweky, M. Enhancing Intubation Accuracy: Advanced Tracheal Segmentation Techniques In Video Endoscopy. In Proceedings of the 2024 IEEE International Conference on Image Processing (ICIP), Abu Dhabi, United Arab Emirates, 27–30 October 2024; pp. 2833–2838.
19. Kaur, A.; Bir, S.; Singh, H. Image Segmentation Using Entropy: A Review. *Int. J. Emerg. Sci. Eng.* **2013**, *2*, 7–9.
20. Saraiva, P. On Shannon entropy and its applications. *Kuwait J. Sci.* **2023**, *50*, 194–199. [CrossRef]
21. Wenqi, J.; Xiaoguang, H. Kapur's Entropy for Multilevel Thresholding Image Segmentation Based on Moth-Flame Optimization. *Math. Biosci. Eng.* **2021**, *18*, 7110–7142. [CrossRef]
22. Fuentes, J.; Gonçalves, J. Rényi Entropy in Statistical Mechanics. *Entropy* **2022**, *24*, 1080. [CrossRef]
23. Alomani, G.; Kayid, M. Further Properties of Tsallis Entropy and Its Application. *Entropy* **2023**, *25*, 199. [CrossRef] [PubMed]
24. Jia, H.; Peng, X.; Song, W.; Oliva, D.; Lang, C.; Li, Y. Masi Entropy for Satellite Color Image Segmentation Using Tournament-Based Lévy Multiverse Optimization Algorithm. *Remote Sens.* **2019**, *11*, 942. [CrossRef]
25. Kumar, N.; Dixit, A.; Vijay, V. Entropy measures and their applications: A comprehensive review. *arXiv* **2025**, arXiv:2503.15660. [CrossRef]
26. Amiriebrahimabadi, M.; Rouhi, Z.; Mansouri, N. A Comprehensive survey of multi-level thresholding segmentation methods for image processing. *Arch. Comput. Methods Eng.* **2024**, *31*, 3647–3697. [CrossRef]
27. Sezgin, M.; Sankur, B. Survey over image thresholding techniques and quantitative performance evaluation. *J. Electron. Imaging* **2004**, *13*, 146–168. [CrossRef]
28. Binney, J. *Entropy: A Very Short Introduction*; Oxford University Press: Oxford, UK, 2025.
29. Kolmogorov, A.N. *Foundations of the Theory of Probability*; Julius Springer: Berlin, Germany, 1933.
30. Burke, C. A century of influence: Part 1. Orthodontic pioneers. *Am. J. Orthod. Dentofac. Orthop.* **2015**, *147*, S155–S160. [CrossRef] [PubMed]
31. Li, M.; Vitányi, P. *Introduction to Kolmogorov Complexity and Its Applications*; Springer: Cham, Switzerland, 2019; pp. XXIII, 834.
32. Wu, Y.; Zhou, Y.; Saveriades, G.; Agaian, S.; Noonan, J.P.; Natarajan, P. Local Shannon entropy measure with statistical tests for image randomness. *Inf. Sci.* **2013**, *222*, 323–342. [CrossRef]
33. Agaian, S. *Visual Morphology (Electronic Imaging '99)*; SPIE: Bellingham, WA, USA, 1999; Volume 3646.
34. Benbelkacem, S.; Oulefki, A.; Agaian, S.; Zenati-Henda, N.; Trongtirakul, T.; Aouam, D.; Masmoudi, M.; Zemmouri, M. COVI3D: Automatic COVID-19 CT Image-Based Classification and Visualization Platform Utilizing Virtual and Augmented Reality Technologies. *Diagnostics* **2022**, *12*, 649. [CrossRef] [PubMed]
35. Pun, T. Entropic thresholding, a new approach. *Comput. Graph. Image Process.* **1981**, *16*, 210–239. [CrossRef]
36. Kapur, J.N.; Sahoo, P.K.; Wong, A.K.C. A new method for gray-level picture thresholding using the entropy of the histogram. *Comput. Vis. Graph. Image Process.* **1985**, *29*, 273–285. [CrossRef]
37. Sahoo, P.; Wilkins, C.; Yeager, J. Threshold selection using Renyi's entropy. *Pattern Recognit.* **1997**, *30*, 71–84. [CrossRef]
38. Anastasiadis, A. Special Issue: Tsallis Entropy. *Entropy* **2012**, *14*, 174–176. [CrossRef]
39. Tsallis, C. Possible Generalization of Boltzmann-Gibbs Statistics. *J. Stat. Phys.* **1988**, *52*, 479–487. [CrossRef]
40. Masi, M. A Step Beyond Tsallis and Rényi Entropies. *Phys. Lett. A* **2005**, *338*, 217–224. [CrossRef]
41. Lin, Q.; Ou, C. Tsallis entropy and the long-range correlation in image thresholding. *Signal Process.* **2012**, *92*, 2931–2939. [CrossRef]
42. Sudakow, I.; Asari, V.K.; Liu, R.; Demchev, D. MeltPondNet: A Swin Transformer U-Net for Detection of Melt Ponds on Arctic Sea Ice. *IEEE J. Sel. Top. Appl. Earth Obs. Remote Sens.* **2022**, *15*, 8776–8784. [CrossRef]
43. Salas-Robles, J.E.; Biot-Monterde, V.; Antonino-Daviu, J.A. Current and Stray Flux Combined Analysis for Sparking Detection in DC Motors/Generators Using Shannon Entropy. *Entropy* **2024**, *26*, 744. [CrossRef] [PubMed]

44. Zhang, K.; He, M.; Dong, L.; Ou, C. The Application of Tsallis Entropy Based Self-Adaptive Algorithm for Multi-Threshold Image Segmentation. *Entropy* **2024**, *26*, 777. [CrossRef]
45. Nomura, R.; Yagi, H. Optimum Achievable Rates in Two Random Number Generation Problems with f-Divergences Using Smooth Rényi Entropy. *Entropy* **2024**, *26*, 766. [CrossRef]
46. Ayunts, H.; Grigoryan, A.; Agaian, S. Novel Entropy for Enhanced Thermal Imaging and Uncertainty Quantification. *Entropy* **2024**, *26*, 374. [CrossRef] [PubMed]
47. Ayunts, H.; Agaian, S.; Grigoryan, A.M. Solar Photovoltaic System Fault Classification via Hierarchical Deep Learning with Imbalanced Multi-Class Thermal Dataset. *Energies* **2026**, *19*, 462. [CrossRef]
48. Oulefki, A.; Agaian, S.; Trongtirakul, T.; Laouar, A.K. Automatic COVID-19 lung infected region segmentation and measurement using CT-scans images. *Pattern Recognit.* **2021**, *114*, 107747. [CrossRef] [PubMed]